ACS Photonics

Article

Cite This: ACS Photonics 2018, 5, 1933−1942

Tailored UV Emission by Nonlinear IR Excitation from ZnO Photonic Crystal Nanocavities

Sandro P. Hoffmann,*[,†] Maximilian Albert,[†] Nils Weber,[†] Denis Sievers,[‡] Jens Förstner,[‡] Thomas Zentgraf,[†] and Cedrik Meier*[,†]

[†]Department of Physics and [‡]Department of Electrical Engineering, Paderborn University & CeOPP, Warburger Straße 100, 33098 Paderborn, Germany

Supporting Information

ABSTRACT: For many applications in photonics, e.g., free-space telecommunication, efficient UV sources are needed. However, optical excitation of such sources requires photons of even higher energies, which are difficult to integrate into photonic circuits. Here, we present photonic crystal devices based on zinc oxide (ZnO) that allow excitation using highly abundant sources in the near-infrared (NIR). These devices offer control of generating tailored photonic modes in the UV range via higher order nonlinear processes by combining the wide electronic band gap and pronounced nonlinear effects in ZnO with the adjustable properties of photonic crystal (PhC) membranes. Two different techniques for fabricating such ZnO-based PhC membranes are discussed, including the presentation of a novel bottom-up approach. Furthermore, dispersive theoretical simulations are introduced to determine the size and position of the photonic band gap, leading to an optimized cavity with only one dominant mode. This is followed by an evaluation of dominant loss channels, comparing cavities for both fabrication techniques, where we implemented a semianalytical model to determine scattering losses at imperfections of the PhCs. Additionally, energetic fine-tuning of such a mode as well as for other photonic modes that are formed by different cavity types is demonstrated. Ultimately, we validate that both linear one-photon and nonlinear three-photon excitation is possible with the presented devices, which renders them potential candidates for efficient UV light emitters that are powered by IR or NIR light sources.

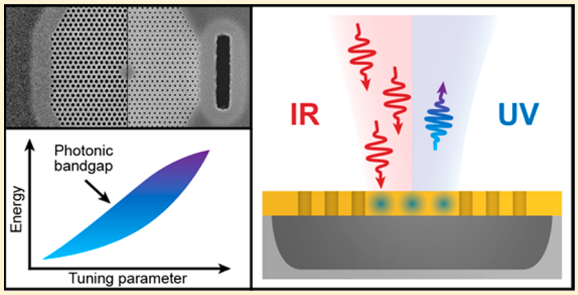

KEYWORDS: *nonlinear IR excitation, multiphoton absorption, tunable UV emission, low-cost UV sources, ZnO photonic crystal membranes, zinc oxide thin films*

Photonic crystals (PhCs) have been the object of intensive research over the past decades, as they are a promising and versatile platform due to highly adaptable 3D light confinement. They allow for tailoring the light propagation by employing many different dielectric materials in a variety of functional designs together with numerous possibilities of combining material-based and photonic effects.[1−3] Consequently, prominent optoelectronic devices emerged, such as PhC-based LEDs[4] and lasers[5] or even biomolecular sensors.[6] By embedding quantum dots,[7] quantum wires,[8,9] or quantum wells,[10] PhCs were introduced in several fundamental fields, for instance, integrated or quantum optics. In the beginning, these structures were primarily realized in Si-, GaAs-, or InP-based material systems,[11−13] since a suspension of a thin membrane by using selective wet-etching to remove the underneath sacrificial layer led to high Q factor values. Further advances in the etching chemistry and growth techniques allowed PhC structures based on wide band-gap semiconductors such as GaN or AlN, enabling new devices and principle investigation in the regime of green to blue wavelengths.[14−16] For the visible to UV region, tailoring and tuning the emission by utilizing GaN-based quantum dots or quantum wells were demonstrated eventually.[17,18]

However, ZnO, while also emitting in the UV range, has an even larger exciton binding energy, ranging from 60 meV for bulk ZnO to about 110 meV for ZnO/(Zn,Mg)O quantum wells,[19] which allows for high-efficiency light emission by improved exciton−photon coupling and the possibility of achieving strong carrier localization, even at room temperature.[20−22] Moreover, ZnO exhibits pronounced nonlinear properties, which makes ZnO-based devices even more applicable not only for room-temperature UV lasers and single-photon sources but also for polariton lasers.[23−26] In addition to that, an efficient multiphoton absorption enables compatibility for integrated circuits with well-developed IR light sources. Besides high availability, the low-energy photons of IR light sources, in contrast to UV, are less likely to be absorbed and thus allow for a variety of materials within a photonic circuit.

Received: October 17, 2017
Published: March 11, 2018

DOI: 10.1021/acsphotonics.7b01228
ACS Photonics 2018, 5, 1933−1942

Although dry etching of ZnO is comparatively difficult and obstacles exist due to the relatively small structure size that is required for UV application, different ZnO-based PhC devices have already been demonstrated. The group of Hui Cao, for instance, demonstrated emission in the UV regime that showed some features of lasing based on defect modes from structural disorder in 2D PhCs out of a ZnO slab on a sapphire substrate.[27,28] Although the PhC is patterned well into the substrate, the poor index contrast only allows for a small photonic band gap (PBG) that is shifted toward lower energies,[29,30] thus requiring the fabrication of even smaller structures. Unfortunately, due to the lack of selective etching chemistry of commonly used ZnO substrates, including sapphire, the fabrication of ZnO-based PhC membranes remains a huge challenge. While the fabrication of 3D PhC opal structures tackled these limitations by providing a larger PBG,[31] these devices are rather difficult to integrate into photonic circuits.

Recently, we reported on a top-down fabrication method, where we addressed these problems and successfully demonstrated, for the first time, a completely free-standing ZnO-based PhC membrane.[32] In this work, we investigate and optimize the 3D light confinement and present an additional fabrication technique for such membranes via a bottom-up approach. We then demonstrate that these devices offer a controlled generation of tailored photonic cavity modes in the UV range and allow excitation using highly abundant sources in the near-infrared (NIR) by combining the adjustable properties of PhC membranes with the aforementioned properties of ZnO. Therefore, this work presents substantial progress in the fabrication of ZnO-based photonic devices that are based on nonlinear optical excitations. The use of Si-based substrates bridges our technology also toward the rapidly developing field of silicon photonics, so that, for example, the integration of low-cost compact IR laser diodes with SiO_2/Si-waveguides and ZnO UV emitter arrays becomes feasible, which could find application as array UV light sources in biotechnology.

The presented two-dimensional photonic crystal nanocavities are all realized in free-standing membranes that feature a 3D confinement of light. In particular, a periodic modulation of the dielectric function by triangularly arranged holes provides in-plane reflection due to the formation of a PBG where propagation is inhibited for a specific range of frequencies or wavelengths. A photonic resonator is then introduced by locally breaking the periodicity. Furthermore, the higher refractive index contrast of the membrane compared to the surrounding air creates a planar optical confinement by total internal reflection. The key feature for easily tailoring this PBG while not replacing the involved materials is the scalability of the PhCs. Assuming a constant relative permittivity, the photonic bands scale linearly with the lattice parameter a.[33−35] By choosing this parameter accordingly, the PBG can be positioned as desired. The width of this gap is determined by the ratio of the two materials used for the periodic modulation along the lattice, often described by the ratio of hole radius and distance, r/a.

Consequently, in this work, the PhCs are arranged in arrays with different lattice constants, in the range of a = 177−197 nm, and varying hole radii between $r = 0.25a$ and $r = 0.42a$. For the experiments, there are two sample types, A and B, respectively. Sample type A is fabricated via a top-down approach; thus, all layers of the heterostructure are grown and deposited primarily and patterned afterward.[32,36] On the other hand, type B samples are realized by a novel bottom-up approach, where prepatterned SiO_2 PhC membranes are overgrown with ZnO. The fabrication and their characterization are described in detail in the Supporting Information.

SIMULATIONS

In order to optimize the PBG in terms of size and energetic position near the electronic band gap of ZnO, the band structure of the SiO_2−ZnO−SiO_2 membrane according to sample type A is simulated. This is achieved by computing the dispersion relation in the frequency domain using the freely available software package MIT Photonic Bands (MPB, see Supporting Information for further details). As stated above, the acquired band structure is scalable with the lattice parameter a of the PhC only for a constant relative permittivity. While this might be a sufficient assumption for SiO_2, this is not accurate for the semiconducting ZnO due to material dispersion in the spectral region near the electronic band gap. Since the simulation via MPB only works with a constant and real permittivity, in principle only nondispersive calculations could be performed. To overcome this limitation, the groups of H. Cao and R. Chang, for instance, calculated a set of band structures for different refractive indices and determined $\omega(n)$ via the intersection of $n_{ZnO}(\omega)$ and interpolated simulation data.[28,37] Here, this method cannot be utilized due to the additional layers of SiO_2 that impact the band structure. For that reason, we implemented an iterative algorithm that works as follows: first, the dielectric functions of the ZnO and SiO_2 layers of the corresponding sample were determined via spectroscopic ellipsometry by fitting an oscillator model to the measured data in the range of 350−1200 nm (see Figure 1, left). The real parts of the fitted dielectric functions for both ZnO and SiO_2 were then implemented into an algorithm. It iteratively calculates the corresponding frequency ω_i, where i is the band index, at the given points in k space with MPB's standard method, thus with a constant relative permittivity, for the SiO_2−ZnO−SiO_2 PhC membrane. The obtained result is

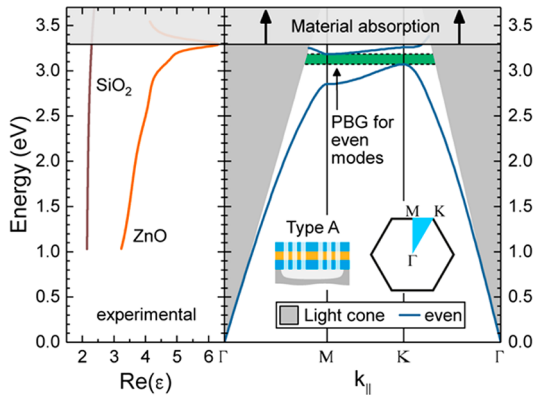

Figure 1. Left: Real parts of the dielectric functions of the involved SiO_2 (brown) and ZnO (orange) layers, experimentally determined by ellipsometry. Right: Dispersive band diagram for a specific PhC (type A, H2 cavity, $r = 0.2574a$, a = 180 nm, at $z = 0$ for even polarization), obtained by implementing the experimental data for the relative permittivity (left graphs) into an iterative algorithm. The formation of a PBG between ∼3.1 and 3.2 eV can be observed. Since only real dielectric functions are accepted by the computation method of MPB, the region with high material absorption above the electronic band gap of ZnO at ∼3.3 eV is marked with a gray overlay.

DOI: 10.1021/acsphotonics.7b01228
ACS Photonics 2018, 5, 1933−1942

then inserted into the fitted dielectric functions, followed by a recalculation of ω_i. This is repeated until the difference for that frequency ω_i compared to the previous result is less than 3 meV. Then, ω_{i+1} is determined the same way, until all frequencies below the light cone are calculated and the next k point is processed in the same manner. This algorithm takes account of the dispersive properties of ZnO and SiO_2 simultaneously; dissipative effects, however, are not considered since MPB accepts only real numbers as permittivity. The obtained band diagram together with the corresponding dielectric functions for a specific PhC with a lattice parameter of a = 180 nm and r = 46.33 nm, which will be further characterized in this paper, is shown in Figure 1.

Although the real part of the dielectric function for SiO_2 (Figure 1, left) increases steadily with higher energies, the deviation is less than 5% in comparison to the constant value of ε_{SiO_2} = 2.2, which is used for the initial nondispersive simulations (see the SI). For ZnO, however, the dielectric function strongly deviates from a constant value of, for example, ε_{ZnO} = 4.5. It has a pronounced maximum at the electronic band gap of ZnO at 3.3 eV with an increasing slope starting at ~3.0 eV, which is attributable to material absorption effects of the electronic band gap of ZnO as well as growth-related electron interface traps at the grain boundaries.[38] A higher permittivity is found to decrease the corresponding eigenfrequencies and thus the photonic bands. As a result, the nondispersive band diagram is compressed toward an energy that corresponds to the constant values for the permittivity that are taken for nondispersive simulations (e.g., see Figure S3, SI).

The band diagram itself (Figure 1, right) exhibits a PBG between the highest point of the first band (~3.19 eV) at the K point and the lowest point of the second band (~3.07 eV) at the M point. This purposely narrow PBG, in order to generate only one photonic mode, is the result of the rather small ratio of r/a = 0.2574. The energetic position of the PBG, as mentioned before, is controlled via the lattice parameter a and is chosen so that the PBG is just below the electronic band gap of the ZnO. The gray area corresponds to all frequencies above the light line $\omega = ck/n$ of the surrounding material (air in this case), the so-called light cone[35,39] (see SI for further details). Since only real dielectric functions are accepted by the computation method of MPB, the region with high material absorption at the electronic band gap of ZnO at ~3.3 eV and above is marked with a gray overlay. In combination with an H2 cavity, this tailored PhC leads to a single dominant cavity mode that is positioned just below the near-band-gap emission (NBE) of ZnO, so that the material absorption will not decrease the quality factor Q of the mode. The characterization and discussion of this PhC device is part of the following section.

EXPERIMENTAL RESULTS

In the previous section, a dispersive model for calculating the photonic band structure was discussed and geometric parameters providing a PhC design for a photonic mode within a narrow PBG near the NBE of ZnO were obtained. This section will present the photoluminescence (PL) results of the completely fabricated PhCs, starting with type A (see SI for a detailed description of the sample types). The cavity performance, namely, the Q factor, is then compared to a similar type B PhC. In the second part of this section, linear UV excitation as well as nonlinear excitation via a NIR source will be utilized to consistently generate adjustable cavity modes from different cavity types.

First, the samples are excited linearly, as described in the Supporting Information, with an excitation wavelength of λ_{exc} = 325 nm. Figure 2 presents the PL spectrum of the previously

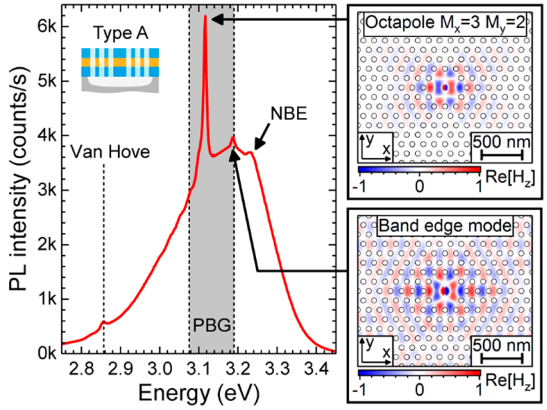

Figure 2. Left: Photoluminescence measurement (cw, confocal setup, λ_{exc} = 325 nm at room temperature) of the PhC discussed in simulations section (type A, H2 cavity, r = 0.2574a and a = 180 nm). Dotted lines correspond to the predicted energies of the Van Hove singularity, the upper and the lower photonic band edge, respectively, taken from the dispersive MPB simulations (see Figure 1). They align almost perfectly with peaks in the measured spectra that are not attributable to the bulk ZnO luminescence, hence an effect of the PhC membrane. Most importantly, a pronounced peak can be observed inside the PBG (Q_{exp} = 329), in agreement with the predictions of the time-domain simulations (see Figure S4a). Right: Field plots of the z-component of the magnetic field, obtained by time-domain simulations. A strong localization inside the cavity can be found for the photonic mode (top), whereas the peak resulting from the upper PBG has a more evenly spread field distribution (bottom). Please note that remainders of the not completely decayed dipole excitation source located in the center of the cavity account for the increased field in the center.

simulated PhC (Figure 1) with an H2 cavity. A prominent feature of this graph is the pronounced photonic mode inside the PBG (gray area) at 3.116 eV, resulting from the three-dimensional optical confinement of the photonic membrane. This is in agreement with the time-domain simulations, where a mode was found also inside the gap. Moreover, smaller peaks are identifiable at the simulated positions, marked with dashed horizontal lines, of the dominant Van Hove singularity (see Figures S3 and S4, SI) at 2.853 eV, the lower band edge at 3.073 eV, and the upper band edge at 3.185 eV, respectively. The NBE of the bulk ZnO is visible as a peak around 3.23 eV, hence slightly above the PBG. This is intended since a PBG around the NBE would be a poor resonator due to the nonzero material absorption that would lead to a reduced Q factor of the photonic mode.[40] By positioning the PBG slightly below that energy, one dominant and sharp photonic resonance with a Q factor of 328 is achieved.

In order to verify a proper localization of this photonic mode, time-domain simulations are performed using narrow excitation pulses with the respective energies of the four discussed peaks that are based on the PhC structure. The z-component of the magnetic field H_z for the cavity mode as well as for the peak at the upper photonic band edge is presented in the inset on the right in Figure 2. It is evident from the plot that the cavity mode is localized inside the cavity, as expected, whereas the

DOI: 10.1021/acsphotonics.7b01228
ACS Photonics 2018, 5, 1933−1942

upper band edge is evenly distributed across the structure. Together, these results demonstrate a good agreement between the utilized methods of simulation and, additionally, a very good control of the rather complex fabrication for type A samples. Furthermore, this cavity mode can be identified as an octapole with three nodal planes along the x and two along the y direction. The higher order of this mode can be explained by the fact that its frequency is much larger than the width of the PBG. Since the lifetime τ of the mode is proportional to its Q factor, the time-domain simulation yields $Q_{intr} = 444$, with a mode volume of $V_{A,eff} = 2.88\ (\lambda/n)^3$.

Loss Evaluations. We start the evaluation of the investigated devices with a theoretical analysis of the main loss contributions. In general, there are many potential loss channels in these photonic devices,[41] such as design and fabrication imperfections that lead to scattering and a poor confinement, which all reduce the Q factor. Since the obtained modes are relatively broad, this analysis concentrates on the ones that, we believe, have the most impact: the intrinsic losses (accounted for in Q_{intr}), the material absorption (Q_{abs}), and the scattering at surface imperfections (Q_{ss}). We obtain the total quality factor from

$$Q_{tot}^{-1} = Q_{intr}^{-1} + Q_{abs}^{-1} + Q_{ss}^{-1} \quad (1)$$

Table 1 summarizes all contributions for the investigated cavities and substrates together with the experimental values for the quality factor (Q_{exp}, averaged over multiple devices).

Table 1. Overview of the Theoretical Quality Factors (Q_{tot}) and the Contributions from Intrinsic Quality Factor (Q_{intr}), Absorption (Q_{abs}), and Surface Scattering (Q_{ss}), Together with the Experimental Quality Factor, Averaged over Multiple Devices (Q_{exp}), and the Effective Mode Volume V_{eff}

	Q_{intr}	Q_{abs}	Q_{ss}	Q_{tot}	Q_{exp}	V_{eff} [$(\lambda/n)^3$]
Type A						
H2	444	191 570	40 191	438	328	2.88
L7	308	191 570	76 041	306		5.12
Type B						
H2	426	112.36	3531	87	239	2.44
L3	553	112.36	3264	91	203	1.96
L7	504	112.36	5169	90	211	2.77

We use time-domain simulations to obtain the intrinsic quality factor Q_{intr} from the cavity mode lifetime τ as already mentioned above. For all cavity/substrate combinations, we see strong radiation losses, leading to overall values for Q_{intr} between 300 and 550. We could not find confined modes for L3 cavities for substrate type A due to the lower ZnO layer thickness for this material. For type B, we find as commonly expected higher values for Q_{intr} for L-type cavities than for H2 cavities.

For the determination of the influence of absorption on the quality factor (Q_{abs}), we take the absorption in the different layers and their respective absorption coefficients into account. As discussed in the Supporting Information, while comparing the ZnO quality of type A and B samples, the bottom-up approach of type B does not allow postgrowth rapid thermal annealing that would strongly enhance the PL in terms of reduced luminescence from defects and grain boundaries.[32,36] As a result, the material absorption in the region of the cavity mode is several magnitudes higher than for type A (see Figure S2c). The resulting loss can be calculated via $Q_{abs}^{-1} = \alpha_{eff}/2\pi n_{eff}$, where $\alpha_{eff} = \sum_i \Gamma_i \alpha_i$ is the effective absorption coefficient as the sum of the amount of field energy Γ_i stored in the respective layer i multiplied with its absorption coefficient. This calculation yields $Q_{A,abs} = 191\ 570$ and $Q_{B,abs} = 112.36$.

For the determination of the loss caused by surface scattering (Q_{ss}), we need to take into account the sidewall taper and roughness of the experimentally fabricated devices. Here, we use experimental SEM data from a large number of photonic crystal holes and perform a statistical analysis based on a Gaussian model. This way, we obtain a correlation length L_C and a standard deviation σ_R. Figure 3a–d show the results for this analysis for substrate types A and B. The correlation length and standard deviation are subsequently used for a semi-analytical approach to estimate the surface scattering quality factor Q_{ss}. The approach works as follows.

We start with the electromagnetic fields of an ideal cavity as obtained from numerical time-domain simulations. Then, we determine the normalized energy density

$$\overline{u}_s = \varepsilon_0 \sum \langle |\vec{E}^0(\hat{\eta})|^2 \rangle_{i,edge} / U_C \quad (2)$$

summed over all photonic crystal hole edges numerically. Here, U_C denotes the total energy derived from the electric and magnetic fields of the unperturbed cavity and $|\vec{E}^0(\hat{\eta})|^2_{i,edge}$ is the electric field intensity averaged along the wall of the photonic crystal hole i. To account for the disorder of the holes, we treat each hole of the photonic crystal individually and compute the radiated power $P_{rad,i}$ for each hole i. Here, we employ a Gaussian model for the correlation of the deviation of the holes from cylindrical shape[42] and use L_C and σ_R from the aforementioned statistical analysis of the SEM data. The complete radiated power due to surface scattering is subsequently computed by summing up over the radiated power for each hole, $P_{rad} = \sum P_{rad,i}$. To compute the radiated power for an individual hole, $P_{rad,i}$, we average over the field intensity along the edge of the photonic crystal hole under the assumption that the field changes slowly within the correlation length, L_C. Thus, $P_{rad,i}$, for a cylindrical photonic crystal hole is computed similarly to eq 29 from Borselli,[42] with the field intensity $|E_m|^2$ of a microdisk mode replaced by the averaged field along the edge for each photonic crystal hole, $|\vec{E}^0(\hat{\eta})|^2_{i,edge}$. The quality factor is finally calculated from $Q_{ss} = \omega U_C / P_{rad}$. It should be noted that this approach does not differentiate between total scattering and backscattering, as considered, for example., by Hughes et al.[43] However, a detailed discussion of all possible loss channels is not in the scope of this paper, since the investigated cavities are dominated by intrinsic or absorption loss.

The results for the surface scattering are shown in Table 1. As expected, the values for Q_{ss} for substrate type A are significantly higher due to the smoother quality of the sidewalls for this fabrication process. The difference in the hole fabrication can also be seen from Figure 3a and c, where the higher disorder for type B is evident. When comparing the different cavity types, the semianalytical values for Q_{ss} also show that the L7 cavity is much more robust against fabrication imperfections than the H2 cavity, which is more strongly affected by surface scattering for both type A and type B substrates. As substrate type A could not support confined modes for L3 cavities, a comparison for this cavity type was not possible.

DOI: 10.1021/acsphotonics.7b01228
ACS Photonics 2018, 5, 1933–1942

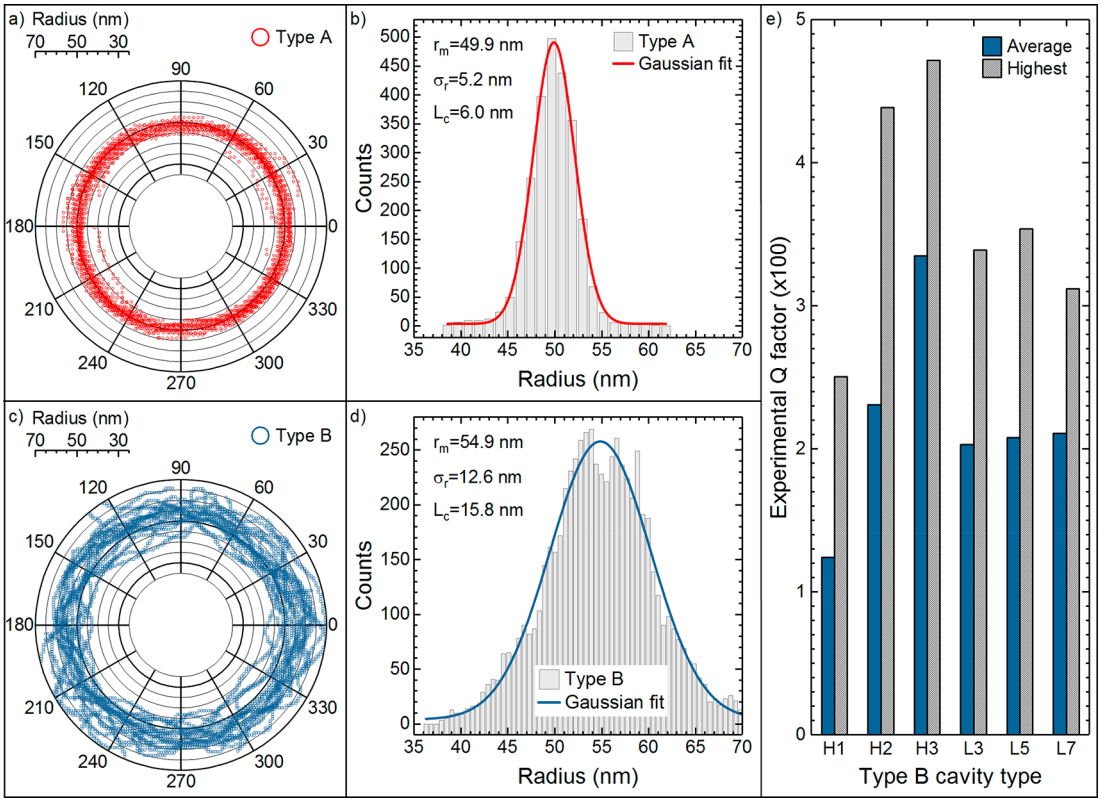

Figure 3. (a–d) Statistical analysis of the hole radius variation due to sidewall taper for two similar type A and B PhCs. The polar plots (a and c) are obtained by analyzing different holes for one specific PhC with an SEM image. The plots are therefore a superposition of all obtained radii $r(\varphi)$ and visualize the deviation from the ideal hole radius. The corresponding histograms (b and d) are fitted to acquire the mean radius and standard distribution. (e) Histogram displaying the experimental Q factors for different cavity types of the type B samples. The gray and dotted bars correspond to the highest measured values, whereas the blue bars reflect the average Q factor of different PhCs.

The theoretical analysis leads to the conclusion that, for the studied cavity/substrate combinations, surface scattering has the least impact on the total quality factor. For substrate type A, the radiative losses are dominant, while for substrate type B, absorption loss is the strongest contribution.

Apart from the different contributions to cavity loss, we also determined the effective mode volumes for each cavity and substrate type. The last column of Table 1 lists the results. We find that, in general, substrate type A leads to larger mode volumes than substrate type B. It is also evident from this calculation that the confinement for L7 cavities is much weaker for type A substrates than for type B. This can be explained by the much thinner high-index ZnO film in type A material in comparison to substrate type B. Moreover, an additional SiO_2 cladding layer on top of the ZnO film in the type A substrates leads to a soft decay of the electromagnetic fields. From the data it is also seen, as expected, that for the linear cavities the mode volume increases with increasing cavity dimension. For the well-confined type B substrates it is also reasonable that the mode volume for L7 and H2 cavities is quite similar, which both consist of an equal number of missing holes from the photonic crystal design.

For the experimental analysis of the loss mechanisms, we compare the performance of the different substrates for H2 cavities, which support confined modes for both type A and type B substrates. Here, the experimental data (Q_{exp} in Table 1) support the theoretical result (Q_{tot} in Table 1) that the quality factors for type A substrates are higher. While for type A substrates the experimental values are in good agreement with the computation, in fact, the experimentally observed quality factors for type B substrates are even higher than predicted. For type B substrates, the theoretical analysis yields absorption loss as the main loss channel. Assuming an error margin of ±5% for the estimation of the absorption coefficient (the absorption of the film was determined by spectroscopic ellipsometry using an oscillator model), the quality factor for absorption Q_{abs} could in fact be larger, and the resulting Q values then cover the experimentally obtained quality factors.

An overview of the experimentally observed averaged quality factors and highest quality factor for each fabricated cavity type is shown in Figure 3e. For the hexagonal cavity, one can see a consistent trend for increasing quality factors with increasing cavity size. This is expected due to the reduced influence of sidewall roughness. Thus, the highest Q factors are achieved with H2 (439) and H3 (472), respectively. For the linear cavities, this effect is much less pronounced. This can be explained by the fact that those cavities only extend into one direction, and thus the influence of sidewall roughness remains.

To summarize the loss mechanisms, we find that type A PhCs are in principle superior to the type B PhCs with respect to a high Q factor, since the latter are more strongly affected by the material absorption and growth-related sidewall taper. On the contrary, the bottom-up approach of the type B samples offers a wider range of possible hole radii ratios r/a that is beneficial for a wide PBG. Furthermore, larger layer thicknesses for both the ZnO and the SiO_2 layer can be achieved, which would increase the Q factor. In addition to that, the type B samples can be fabricated much faster and more reliably.

DOI: 10.1021/acsphotonics.7b01228
ACS Photonics 2018, 5, 1933–1942

Tailored Linear and Nonlinear UV Emission. Increasing the hole radius is supposed to lead to a shift of the examined PBG (e.g., see inset in Figure S3), thus the previously discussed photonic mode (Figure 2), toward higher energies. In Figure 4a, PL measurements of PhCs with different radii ranging from

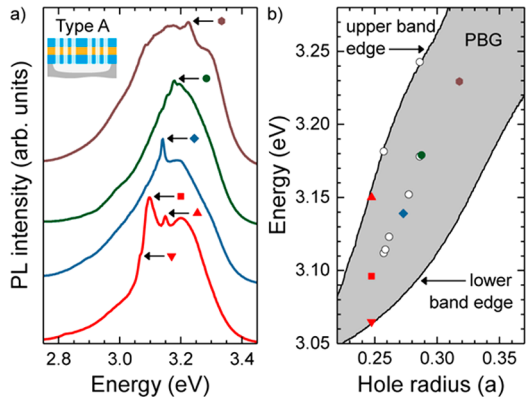

Figure 4. (a) Photoluminescence measurement (cw, confocal setup, λ_{exc} = 325 nm at room temperature) of PhCs with different hole radii (r = [0.2476–0.3180]a, type A, H2 cavity and a = 180 nm) that lead to a shift of the PBG and photonic modes. For a better distinguishability, the graphs are stacked lowest (red, bottom graph) to highest radius and normalized with respect to their intensity maximum. The pronounced photonic modes are marked with symbols. (b) Corresponding dispersive simulation of the upper and lower band edge energies for different radii. The colored symbols mark the energetic position together with the measured radius of their counterparts in (a). Additionally, the positions of these characteristic peaks in not shown spectra are added with hollow circles. All identified peaks follow the slope of the PBG.

r = 0.2476a to r = 0.3180a are presented. All PhCs are fabricated with a lattice constant of a = 180 nm and an H2 cavity. The bottom graph (red) with the smallest radius is similar to the discussed graph in Figure 2 in terms of the shape and position of the relevant peaks. Different symbols mark the peaks that result from the PBG as well as the main peak, classified as photonic mode. These three points can also be found with respect to their energies in Figure 4b, where a dispersive simulation of the edges of the PBG for different hole radii is shown (gray area). Here, they align almost perfectly with the simulated graph: the PBG edges are at their respective positions in the graph, together with the photonic mode, which is found between these two points. Again, this demonstrates a very good accordance of experimental data and the theoretical modeling and renders the implemented dispersive algorithm, which is based on the dielectric functions of the involved materials, as convenient for tailoring the PBG.

For the other three graphs in Figure 4a, a shift of the dominant mode toward higher energies can clearly be observed. The respective peaks are again identified with symbols that are also plotted in Figure 4b. Two key features can be observed here: First, the energetic positions of the pronounced peaks follow the slope of the PBG. Second, the intensity and the Q factor of the modes are decreasing with a PBG at higher energies, therefore with increasing material absorption, as described previously in this section. Regardless, this demonstrates the possibility of tuning the photonic mode by tailoring the properties of the PhC with a variation of the hole radius in this instance.

In order to accomplish this tailored UV emission also by IR excitation, multiphoton absorption PL measurements are performed for investigating the nonlinear response of these ZnO-based PhC membranes. The results for a type B PhC with an H2 cavity are presented in Figure 5, where the black graphs

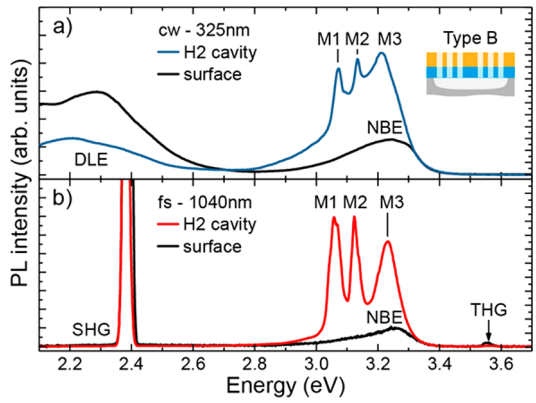

Figure 5. Photoluminescence measurements of a single type B PhC (r = 0.365a, H2 cavity and a = 187 nm) in a confocal setup at room temperature. (a) Spectra of the linear PL (cw, λ_{exc} = 325 nm, 1PA) with deep level emission (DLE) around 2.2 eV and near-band-gap emission (NBE) of ZnO around 3.25 eV. Photonic modes are observable on the low-energy side of the NBE for excitation at the cavity. (b) Multiphoton absorption PL spectra (fs pulse, λ_{exc} = 1040 nm) of the same PhC. Typical features of a nonlinear excitation of ZnO are visible, such as the dominant peak due to second-harmonic generation (SHG) at 2.38 eV or third-harmonic generation (THG) at 3.58 eV, while the DLE is suppressed. Likewise, sharp peaks are present at the same energetic position as for the linear excitation of the cavity just below the NBE at around 3.25 eV. The modes are identified via time-domain simulations with respect to their nodal planes with M1, octupole (M_x = 3, M_y = 2); M2, octupole (M_x = 2, M_y = 3); and M3, dodecapole (M_x = 5, M_y = 4).

correspond to a reference measurement at a nonpatterned area and the colored graphs show the obtained PL for the PhCs. For the surface measurement, the NBE of ZnO is observable around 3.25 eV for both the linear and the nonlinear excitation. When excited with a continuous wave (cw) of 325 nm (see Figure 5a), a deep level emission (DLE) around 2.2 eV becomes apparent that shows a higher intensity for the reference measurement at the surface than for the photonic cavity. Furthermore, three dominant photonic modes are observable on the low-energy side of the NBE for excitation at the cavity. These modes are also observed in corresponding time-domain simulations. From the field distributions inside the cavity, the modes can be identified with respect to their nodal planes as M1, octupole (M_x = 3, M_y = 2); M2, octupole (M_x = 2, M_y = 3); and M3, dodecapole (M_x = 5, M_y = 4). In contrast to the PhC studied in the previous paragraphs, an increased hole radius of r = 0.365a results in a wider PBG that, in addition, is slightly shifted toward lower energies due to the larger lattice parameter of a = 187 nm and the increased ZnO layer height of 57 ± 3 nm.

The same PhC is then excited with pulsed laser peaks of 1040 nm wavelength (~1.19 eV) so that multiphoton absorption is utilized for excitation of the membranes. The obtained PL (Figure 5b) displays typical features of a nonlinear excitation of ZnO such as dominant peaks due to second-harmonic generation (SHG) at 2.38 eV or third-harmonic generation (THG) at 3.58 eV, while the DLE is suppressed due

DOI: 10.1021/acsphotonics.7b01228
ACS Photonics 2018, 5, 1933–1942

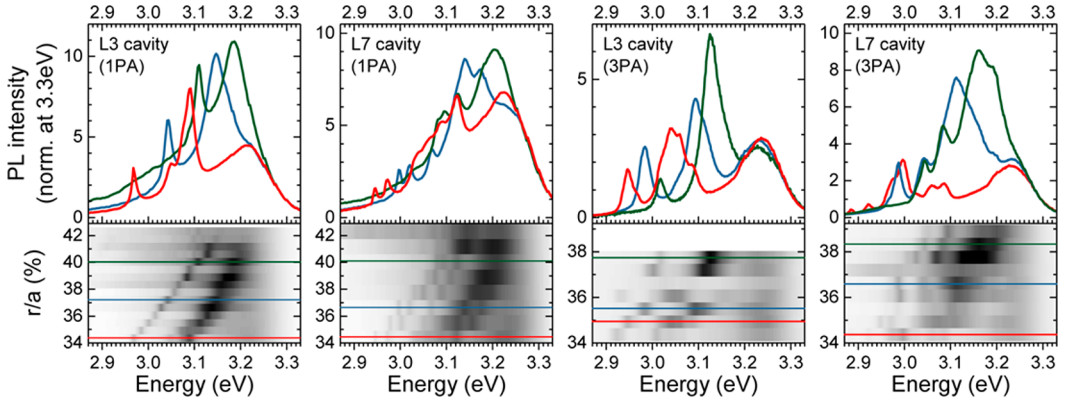

Figure 6. Multiphoton PL experiments on type B samples for radii ranging from $r = 0.344a$ to $r = 0.423a$ with $a = 197$ nm for sample type B with L3 and L7 cavities. Bottom: Intensity plots (black = high, white = low intensity) of all PL measurements with respect to their hole radius. A shift of the black areas, identifiable as photonic modes, toward higher energies with increasing hole size is visible, in agreement with the shift of the PBG. Top: Three exemplary PL spectra for radii corresponding to the colored intersection lines are shown above. The PL spectra are normalized at 3.3 eV for a better comparison of the mode shifts.

to a finite density of defect states.[44] Since the main emission spectrum of ZnO is between these energies, the excitation of electrons from the valence band into the conduction band is attributable to the simultaneous absorption of three photons with the exact same energy. As for the cw excitation, the formation of three dominant peaks on the low-energy side of the NBE can be observed for the cavity excitation. The direct comparison between the one-photon absorption (1PA) and three-photon absorption (3PA) PL reveals a matching energetic position and a number of dominant photonic modes. However, from the 3PA PL it can be seen that, in each case, these modes are a superposition of at least three peaks, where the respective central peak exhibits the highest intensity. This is most likely attributable to the variation of the hole radii through sidewall taper (see Figure 3c and d). Moreover, the dominant peaks on the right in both spectra are superimposed to the NBE, leading to a highly increased intensity at that point compared to the bulk ZnO emission. By designing a PBG with modes only in this energy region, one might obtain an enhanced NBE via PhC membranes.

To conclusively demonstrate tailored UV emission by nonlinear IR excitation, Figure 6 displays the PL results for type B PhCs with L3 and L7 cavities, where the hole radius is varied between $r = [0.344–0.423]a$ while the lattice constant of $a = 197$ nm remains constant. The outcome is expected to be similar to the results shown in Figure 4 and Figure 5. However, the photonic modes are able to form in a broader energy range since the lattice constant is even larger, leading to a wider PBG at lower energies due to the dispersion relations of the materials. Indeed, numerous modes can be observed from both the linear 1PA as well as the nonlinear 3PA spectra. Furthermore, the examined L7 cavity enables the formation of even more photonic modes than for the L3 cavity due to the reciprocal relation between the mode spacing and the cavity size.[45] For the sake of clarity, only three respective 2D graphs of the measured PL are shown at the top of Figure 6 for comparison of shape and position shift of the photonic modes. The spectra for the remaining PhCs with respect to their hole radius are shown in intensity plots at the bottom of Figure 6, where black conforms to the highest and white to the lowest intensity. By this presentation method, a shift of the black areas, identifiable as photonic modes, toward higher energies with increasing hole size becomes apparent more easily. As discussed above, this shift is induced by the shift of the PBG.

For instance, in the plot for the L3 cavity, excited via 1PA, the mode with the lowest energy of about 2.95 eV can clearly be identified in both the intensity plot at the bottom and the corresponding graph (red) above. This mode can also be found at higher energies in the PL spectra for increased hole radii, at 3.04 eV for the blue and at 3.11 eV for the green graph to be specific. This mode can be distinguished from the bulk ZnO PL up to the third to the last plot, which corresponds to a radius of $r = 0.412a$. Since the spectra for the L7 cavity show the same behavior, this can be defined as the maximal feasible radius. Above, the material grid of the PhC is much smaller at the direct connection of the holes along the PhC lattice than the smallest grown ZnO grains, leading to a degraded circularity of the holes and, consequently, a poor optical confinement. A second dominant mode for the 1PA measurement of the L3 cavity can be observed in the discussed spectra at around 3.09 eV (red), 3.15 eV (blue), and 3.19 eV (green), respectively. Likewise, the intensity plot reveals a shift toward higher energies with an increased hole radius. When the mode approaches the energy of the NBE, the intensity weakens due to a reduced Q factor by absorption effects, in agreement with previous results (see Figure 4a). The same overall behavior can be observed from the 1PA of the L7 cavity, but with an ensemble of modes due to the smaller mode spacing for this cavity. As for the 3PA PL, the same trend is recognizable, although it is more difficult to assign the same modes for all radii since the intensity is varying and different modes are pronounced along the series of measurements. This is mainly due to the experimental setup for the nonlinear experiments, where the focal distance is controlled by a differential micrometer screw. Since the PhC membranes respond very sensitively to a change of the laser spot position in all three spatial directions, a well-aimed excitation of specific modes is rather difficult. Regardless, the experiments demonstrate the possibility of fine-tuning photonic modes in a controlled manner, even near the electronic band gap of ZnO, by introducing tailored PhC membrane cavities of different well-known types.

DOI: 10.1021/acsphotonics.7b01228
ACS Photonics 2018, 5, 1933–1942

DISCUSSION

For enhancing the spontaneous emission via resonance-based effects, a reasonably good fine-tuning of the photonic modes may be crucial. The utilized electron beam lithography provides a high patterning fidelity, enabling an adjustment of the lattice parameter a with a precision of about 1 nm. For comparison, the smallest possible lattice parameter variation for the first ZnO-based UV photonic crystal laser, that was presented by the group of Hui Cao, was limited by the resolution of the focused ion beam to 15 nm.[27] In addition to that, our presented devices can be excited in a linear or nonlinear regime by one- to three-photon absorption due to the pronounced nonlinear properties of ZnO, allowing for excitation by IR light sources. This is a huge advantage when compared to similar devices in the UV regime that generally offer higher Q factors. For instance, the group of Yasuhiko Arakawa achieved a mode with $Q = 2400$ at 3.33 eV by embedding GaN QDs inside an AlN PhC membrane[15] (similar to type A). However, this method depends on both spatial and spectral matching between the quantum dot exciton dipoles and the cavity mode. In addition to that, structuring of the involved materials seems rather difficult and complex. In that regard, D. Néel et al. presented also GaN-QD-based PhC membranes out of AlN that were fabricated via a bottom-up approach (similar to type B) by growing AlN on prepatterned silicon.[16] By optimizing an L3 cavity via shifted air holes at the end of the defect, they achieved an optimized Q factor of 1800 at 2.91 eV. This approach is very similar to the presented type B approach, which relies on prepatterned SiO_2 PhCs. They, however, stated that without the cavity optimization the same mode was hardly observed. A respective optimization could also be integrated in our approaches, which would lead to a strongly increased Q factor,[46] independent of statistically distributed QDs and with the capability of nonlinear excitation. Recently, S. Sergent et al. very successfully pursued another hybrid approach, where grooved SiN photonic crystals in combination with ZnO nanowires led to Q factors higher than 2100, which is a remarkable achievement for ZnO. These devices also exploit the highly developed IR technology and possibly can also be excited via NIR and IR sources. However, the fabrication, which involves positioning of the ZnO nanowires via an AFM cantilever, comes with tremendous effort. To conclude, we believe that by utilizing the well-developed Si-based technology together with the pronounced nonlinearities of ZnO, our presented devices have a high potential for low-cost optoelectronic devices.

CONCLUSION

Fully free-standing ZnO-based PhC membranes with hexagonal air holes are presented. Two different approaches for the fabrication allow for hole radii ranging from $r = [0.24-0.42]a$ with lattice constants of $a = 177-197$ nm. For a determination of the size and energetic position of the PBG, a dispersive algorithm is introduced to the theoretical simulation in the frequency domain that uses the relative permittivities of the involved materials, which are obtained via spectroscopic ellipsometry. Consequently, a well-designed PhC membrane with an H2 cavity is fabricated, which exhibits only one dominant mode in the region just below the electronic band gap of ZnO. By varying the hole size, energy shifts of this pronounced mode are demonstrated in excellent agreement with the dispersive simulation. Moreover, analogous energetic fine-tunings of an ensemble of photonic modes is presented for different cavity types in a broad range of hole radii by adjusting the PhC lattice in terms of a larger lattice constant a.

Most importantly, the presented ZnO-based PhCs feature consistent linear and nonlinear excitation via one- and three-photon absorption. This enables the use of IR or NIR light sources for tailored UV emission, which opens a broad range of possible applications in the field of integrated optics and photonics. In combination with the use of well-developed Si-based technology, the presented devices contribute toward the development of low-cost optoelectronic devices.

ASSOCIATED CONTENT

Supporting Information

The Supporting Information is available free of charge on the ACS Publications website at DOI: 10.1021/acsphotonics.7b01228.

Detailed description of the fabrication processes; short comparison between type A and B PhCs with respect to influences of structural imperfections on the Q factor (PL spectra, sidewall taper evaluation); information on the simulation methods (nondispersive band diagram and time-domain spectra); details on the used spectroscopy setups (photoluminescence and ellipsometry) (PDF)

AUTHOR INFORMATION

Corresponding Authors

*E-mail: sandro.hoffmann@upb.de.
*E-mail: cedrik.meier@upb.de.

ORCID

Sandro P. Hoffmann: 0000-0001-7662-6964
Jens Förstner: 0000-0001-7059-9862
Thomas Zentgraf: 0000-0002-8662-1101

Author Contributions

S.P.H. designed and fabricated the PhC crystal membranes, simulated the band diagrams, implemented the dispersive algorithm, performed the photoluminescence measurements, analyzed and evaluated the data, and wrote the manuscript. M.A. and S.P.H. did the ellipsometry measurement; additionally, M.A. fitted the dielectric function. D.S. performed the time-domain simulations. J.F. implemented the semianalytical model for the loss evaluation. N.W. helped with the initial PL setup for the IR excitation, performed further time-domain simulations, and was involved in the Q factor calculation. C.M. supervised the overall project, computed the mode volumes, and contributed to the discussion of loss channels. All authors participated in discussions and revised the manuscript.

Notes

The authors declare no competing financial interest.

ACKNOWLEDGMENTS

This work was support by the Evangelisches Studienwerk e.V. and by the Deutsche Forschungsgemeinschaft (DFG) via grant SFB TRR 142 and GRK 1464.

REFERENCES

(1) Noda, S.; Fujita, M.; Asano, T. Spontaneous-Emission Control by Photonic Crystals and Nanocavities. *Nat. Photonics* **2007**, *1*, 449−458.
(2) Soljačić, M.; Joannopoulos, J. D. Enhancement of Nonlinear Effects Using Photonic Crystals. *Nat. Mater.* **2004**, *3*, 211−219.

DOI: 10.1021/acsphotonics.7b01228
ACS Photonics 2018, 5, 1933−1942

(3) Deotare, P. B.; McCutcheon, M. W.; Frank, I. W.; Khan, M.; Lončar, M. High Quality Factor Photonic Crystal Nanobeam Cavities. *Appl. Phys. Lett.* **2009**, *94*, 121106.
(4) Meier, M.; Mekis, A.; Dodabalapur, A.; Timko, A.; Slusher, R. E.; Joannopoulos, J. D.; Nalamasu, O. Laser Action from Two-Dimensional Distributed Feedback in Photonic Crystals. *Appl. Phys. Lett.* **1999**, *74*, 7−9.
(5) Matioli, E.; Rangel, E.; Iza, M.; Fleury, B.; Pfaff, N.; Speck, J.; Hu, E.; Weisbuch, C. High Extraction Efficiency Light-Emitting Diodes Based on Embedded Air-Gap Photonic-Crystals. *Appl. Phys. Lett.* **2010**, *96*, 96.
(6) Pal, S.; Fauchet, P. M.; Miller, B. L. 1-D and 2-D Photonic Crystals as Optical Methods for Amplifying Biomolecular Recognition. *Anal. Chem.* **2012**, *84*, 8900−8908.
(7) Yoshie, T.; Scherer, A.; Hendrickson, J.; Khitrova, G.; Gibbs, H. M.; Rupper, G.; Ell, C.; Shchekin, O. B.; Deppe, D. G. Vacuum Rabi Splitting with a Single Quantum Dot in a Photonic Crystal Nanocavity. *Nature* **2004**, *432*, 200−203.
(8) Atlasov, K. A.; Karlsson, K. F.; Deichsel, E.; Rudra, A.; Dwir, B.; Kapon, E. Site-Controlled Single Quantum Wire Integrated into a Photonic-Crystal Membrane Microcavity. *Appl. Phys. Lett.* **2007**, *90*, 153107.
(9) Sergent, S.; Takiguchi, M.; Tsuchizawa, T.; Yokoo, A.; Taniyama, H.; Kuramochi, E.; Notomi, M. Nanomanipulating and Tuning Ultraviolet ZnO-Nanowire-Induced Photonic Crystal Nanocavities. *ACS Photonics* **2017**, *4*, 1040−1047.
(10) Fujita, M.; Takahashi, S.; Tanaka, Y.; Asano, T.; Noda, S. Simultaneous Inhibition and Redistribution of Spontaneous Light Emission in Photonic Crystals. *Science (Washington, DC, U. S.)* **2005**, *308*, 1296−1298.
(11) Krauss, T. F.; La Rue, R. M. D.; Brand, S. Two-Dimensional Photonic-Bandgap Structures Operating at near-Infrared Wavelengths. *Nature* **1996**, *383*, 699−702.
(12) Loncar, M.; Doll, T.; Vuckovic, J.; Scherer, A. Design and Fabrication of Silicon Photonic Crystal Optical Waveguides. *J. Lightwave Technol.* **2000**, *18*, 1402−1411.
(13) Park, H.-G.; Kim, S.-H.; Kwon, S.-H.; Ju, Y.-G.; Yang, J.-K.; Baek, J.-H.; Kim, S.-B.; Lee, Y.-H. Electrically Driven Single-Cell Photonic Crystal Laser. *Science (Washington, DC, U. S.)* **2004**, *305*, 1444−1447.
(14) Choi, Y.-S.; Hennessy, K.; Sharma, R.; Haberer, E.; Gao, Y.; DenBaars, S. P.; Nakamura, S.; Hu, E. L.; Meier, C. GaN Blue Photonic Crystal Membrane Nanocavities. *Appl. Phys. Lett.* **2005**, *87*, 243101.
(15) Arita, M.; Ishida, S.; Kako, S.; Iwamoto, S.; Arakawa, Y. AlN Air-Bridge Photonic Crystal Nanocavities Demonstrating High Quality Factor. *Appl. Phys. Lett.* **2007**, *91*, 51106.
(16) Néel, D.; Sergent, S.; Mexis, M.; Sam-Giao, D.; Guillet, T.; Brimont, C.; Bretagnon, T.; Semond, F.; Gayral, B.; David, S.; Checoury, X.; Boucaud, P. AlN Photonic Crystal Nanocavities Realized by Epitaxial Conformal Growth on Nanopatterned Silicon Substrate. *Appl. Phys. Lett.* **2011**, *98*, 261106.
(17) Triviño, N. V.; Butté, R.; Carlin, J. F.; Grandjean, N. Continuous Wave Blue Lasing in III-Nitride Nanobeam Cavity on Silicon. *Nano Lett.* **2015**, *15*, 1259−1263.
(18) Mei, Y.; Weng, G.-E.; Zhang, B.-P.; Liu, J.-P.; Hofmann, W.; Ying, L.-Y.; Zhang, J.-Y.; Li, Z.-C.; Yang, H.; Kuo, H.-C. Quantum Dot Vertical-Cavity Surface-Emitting Lasers Covering the "green Gap. *Light: Sci. Appl.* **2017**, *6*, e16199.
(19) Makino, T. Optical Properties of ZnO-Based Quantum Structures. *Superlattices Microstruct.* **2005**, *38*, 231−244.
(20) Sturm, C.; Hilmer, H.; Schmidt-Grund, R.; Grundmann, M. Observation of Strong Exciton−photon Coupling at Temperatures up to 410 K. *New J. Phys.* **2009**, *11*, 73044.
(21) Kröger, P.; Ruth, M.; Weber, N.; Meier, C. Carrier Localization in ZnO Quantum Wires. *Appl. Phys. Lett.* **2012**, *100*, 263114.
(22) Halm, S.; Kalusniak, S.; Sadofev, S.; Wünsche, H.-J.; Henneberger, F. Strong Exciton-Photon Coupling in a Monolithic ZnO/(Zn,Mg)O Multiple Quantum Well Microcavity. *Appl. Phys. Lett.* **2011**, *99*, 181121.
(23) Zamfirescu, M.; Kavokin, A.; Gil, B.; Malpuech, G.; Kaliteevski, M. ZnO as a Material Mostly Adapted for the Realization of Room-Temperature Polariton Lasers. *Phys. Rev. B: Condens. Matter Mater. Phys.* **2002**, *65*, 161205.
(24) Guillet, T.; Brimont, C.; Valvin, P.; Gil, B.; Bretagnon, T.; Médard, F.; Mihailovic, M.; Zúñiga-Pérez, J.; Leroux, M.; Semond, F.; Bouchoule, S. Laser Emission with Excitonic Gain in a ZnO Planar Microcavity. *Appl. Phys. Lett.* **2011**, *98*, 211105.
(25) Lu, T.-C.; Lai, Y.-Y.; Lan, Y.-P.; Huang, S.-W.; Chen, J.-R.; Wu, Y.-C.; Hsieh, W.-F.; Deng, H. Room Temperature Polariton Lasing vs Photon Lasing in a ZnO-Based Hybrid Microcavity. *Opt. Express* **2012**, *20*, 5530.
(26) Lai, Y.-Y.; Chen, J.-W.; Chang, T.-C.; Chou, Y.-H.; Lu, T.-C. Manipulation of Exciton and Photon Lasing in a Membrane-Type ZnO Microcavity. *Appl. Phys. Lett.* **2015**, *106*, 131106.
(27) Wu, X.; Yamilov, A.; Liu, X.; Li, S.; Dravid, V. P.; Chang, R. P. H.; Cao, H. Ultraviolet Photonic Crystal Laser. *Appl. Phys. Lett.* **2004**, *85*, 3657−3659.
(28) Yamilov, A.; Wu, X.; Liu, X.; Chang, R. P. H.; Cao, H. Self-Optimization of Optical Confinement in an Ultraviolet Photonic Crystal Slab Laser. *Phys. Rev. Lett.* **2006**, *96*, 2−5.
(29) Yamilov, A.; Wu, X.; Cao, H. Photonic Band Structure of ZnO Photonic Crystal Slab Laser. *J. Appl. Phys.* **2005**, *98*, 103102.
(30) Aad, R.; Divay, L.; Bruyant, A.; Blaize, S.; Couteau, C.; Rogers, D. J.; Lerondel, G. Leaky Mode Analysis of Luminescent Thin Films: The Case of ZnO on Sapphire. *J. Appl. Phys.* **2012**, *112*, 112.
(31) Scharrer, M.; Wu, X.; Yamilov, A.; Cao, H.; Chang, R. P. H. Fabrication of Inverted Opal ZnO Photonic Crystals by Atomic Layer Deposition. *Appl. Phys. Lett.* **2005**, *86*, 151113.
(32) Hoffmann, S. P.; Albert, M.; Meier, C. Fabrication of Fully Undercut ZnO-Based Photonic Crystal Membranes with 3D Optical Confinement. *Superlattices Microstruct.* **2016**, *97*, 397−408.
(33) Yablonovitch, E. Photonic Band-Gap Structures. *J. Opt. Soc. Am. B* **1993**, *10*, 283.
(34) Joannopoulos, J. D.; Villeneuve, P. R.; Fan, S. Photonic Crystals. *Solid State Commun.* **1997**, *102*, 165−173.
(35) Johnson, S.; Joannopoulos, J. Block-Iterative Frequency-Domain Methods for Maxwell's Equations in a Planewave Basis. *Opt. Express* **2001**, *8*, 173−190.
(36) Ruth, M.; Meier, C. Structural Enhancement of ZnO on SiO2 for Photonic Applications. *AIP Adv.* **2013**, *3*, 72114.
(37) Scharrer, M.; Yamilov, A.; Wu, X.; Cao, H.; Chang, R. P. H. Ultraviolet Lasing in High-Order Bands of Three-Dimensional ZnO Photonic Crystals. *Appl. Phys. Lett.* **2006**, *88*, 3−5.
(38) Ruth, M.; Meier, C. Scaling Coefficient for Three-Dimensional Grain Coalescence of ZnO on Si(111). *Phys. Rev. B: Condens. Matter Mater. Phys.* **2012**, *86*, 224108.
(39) Meade, R. D.; Brommer, K. D.; Rappe, A. M.; Joannopoulos, J. D. Existence of a Photonic Band Gap in Two Dimensions. *Appl. Phys. Lett.* **1992**, *61*, 495−497.
(40) Akahane, Y.; Asano, T.; Song, B.; Noda, S. Fine-Tuned High-Q Photonic-Crystal Nanocavity. *Opt. Express* **2005**, *13*, 1202−1214.
(41) Yamaguchi, Y.; Jeon, S.; Song, B.-S.; Tanaka, Y.; Asano, T.; Noda, S. Analysis of Q-Factors of Structural Imperfections in Triangular Cross-Section Nanobeam Photonic Crystal Cavities. *J. Opt. Soc. Am. B* **2015**, *32*, 1792−1796.
(42) Borselli, M.; Johnson, T. J.; Painter, O. Beyond the Rayleigh Scattering Limit in High-Q Silicon Microdisks: Theory and Experiment. *Opt. Express* **2005**, *13*, 1515.
(43) Hughes, S.; Ramunno, L.; Young, J. F.; Sipe, J. E. Extrinsic Optical Scattering Loss in Photonic Crystal Waveguides: Role of Fabrication Disorder and Photon Group Velocity. *Phys. Rev. Lett.* **2005**, *94*, 33903.
(44) Bader, C. A.; Zeuner, F.; Bader, M. H. W.; Zentgraf, T.; Meier, C. Nonlinear Optical Sub-Bandgap Excitation of ZnO-Based Photonic Resonators. *J. Appl. Phys.* **2015**, *118*, 213105.

DOI: 10.1021/acsphotonics.7b01228
ACS Photonics 2018, 5, 1933−1942

(45) Okano, M.; Yamada, T.; Sugisaka, J.; Yamamoto, N.; Itoh, M.; Sugaya, T.; Komori, K.; Mori, M. Analysis of Two-Dimensional Photonic Crystal L-Type Cavities with Low-Refractive-Index Material Cladding. *J. Opt.* **2010**, *12*, 75101.
(46) Portalupi, S. L.; Galli, M.; Reardon, C.; Krauss, T.; O'Faolain, L.; Andreani, L. C.; Gerace, D. Planar Photonic Crystal Cavities with Far-Field Optimization for High Coupling Efficiency and Quality Factor. *Opt. Express* **2010**, *18*, 16064.

DOI: 10.1021/acsphotonics.7b01228
ACS Photonics 2018, 5, 1933−1942